Feasibility of multi-aperture µPTV for wall shear stress measurements

Joachim Klinner*, Christian Willert

1: Dept. Engine Measurement Systems, Institute of Propulsion Technology, DLR, Köln, Germany
*Corresponding author: joachim.klinner@dlr.de

Keywords: wall shear stress, multi aperture micro PTV, defocused imaging, turbulent boundary layer, aperture encoding.

ABSTRACT

We present a feasibility study on 3d-3c micro particle tracking velocimetry (µPTV) for boundary layer flows using a single high-speed camera with a microscope lens. Multi-aperture µPTV (MA-µPTV) relies on the "defocusing" concept (Willert & Gharib, 1992) and determines the wall distance of a particle from the size of projected particle image triplets generated by placing a triplet aperature on the entrance pupil of the microscope lens. Illumination with a high-speed pulsed laser is introduced through the same window used for imaging. The calibration of the orientation and size of the particle image triplets is described and accounts for variation of both lateral image position as well as wall distance. Geometrically constrained templates of 2d Gaussians are used to provide least square fitting of triple image intensities, thereby iteratively improving the initial centers and depth position of each particle. In addition, the convolution of a Gaussian and a Lorentzian is studied, that latter of which is considered promising for modeling defocused particle images at large distances from the focus. Lagrangian particle tracks are reconstructed from 3d particle positions using state-of-the-art tracking procedures. The measurement technique is demonstrated in a developing turbulent duct flow of a small wind tunnel up to Re_τ=836 for a wall-bounded volume up to 1.7×1.3×1 mm^3 (in viscous units 52×40 ×31). Comparative profile-PIV measurements provide reference measurements including estimates of the wall shear stress. A comparison with flow statistics obtained with 2d-2c PIV is made possible by bin-averaging the velocities of the particle tracks in the wall-normal direction at a resolution of 10–16 µm. Mean wall shear rates obtained from MA-µPTV and single-line cross-correlation on the PIV data are in good agreement. The fluctuations in wall shear rate are consistent with correlations found in the literature. Statistics from bin-averaged velocities of all tracked particles indicate consistency with profile-PIV and are in agreement with DNS data up to wall distances of 28 viscous units.

1. Introduction

To improve the physical understanding of the turbulent boundary layer (TBL) and to determine viscous scaling parameters as the wall shear stress and friction velocity, measurement techniques that directly measure the fluctuating wall shear-stress can make an important contribution. Among others, the characterization of skin-friction and flow separation, the localization of laminar-turbulent

transition and the detection of sudden reverse-flow events in TBLs with zero-pressure gradient or mild adverse pressure gradient are also of significant relevance.

In addition to film-based techniques, non-contact, tracer-based optical measurement techniques such as digital holographic methods (Sheng et al., 2008) and defocusing micro particle tracking velocimetry (μPTV) (Fuchs, 2019)) along with astigmatism μPTV (Chen et al., 2009; Cierpka et al., 2010) have the potential of providing time-resolved 3d-3c velocity data and feature a relatively low hardware complexity using a single high-speed camera and a combined optical access for both tracer illumination and imaging. A single-axis arrangement was also used by Kumar & Hong (2018); Kumar et al. (2021) to image particles in liquid flow using digital fresnel reflection holography (DFRH).

The tracer based technique proposed herein is aimed at applications in air flows but is equally applicable in liquid flows. The approach relies on depth encoding by multiple-aperture imaging with a microscope lens. Depicted in Fig. 1 the configuration is similar to the concept of *defocusing particle image velocimetry* as introduced by Willert & Gharib (1992). To avoid confusion with *defocusing* μPTV the term multi-aperture micro particle tracking velocimetry (MA-μPTV) is used to describe the imaging setup proposed herein. Since the measurement volume is imaged directly through the glass wall, issues that would normally arise with side-viewing configurations such as parallax and perspective errors due to the slight oblique viewing angle (Cierpka et al., 2013) are mitigated with MA-μPTV.

For defocusing PTV (Fuchs, 2019), the sensitivity, i.e. the ratio of diameter change to depth change, depends mainly on the numerical aperture and the magnification of the microscope objective. A high on-axis sensitivity also requires high beam divergence, which in turn limits the depth of the measurable volume due to rapidly decreasing particle image intensities. Further challenges arise in the accurate determination of the particle diameter away from the focal plane, since in addition to the rapidly deteriorating particle image intensities, the particle image shape can deviate significantly from the ideal diffraction limited Airy disc with halos forming around particle images (Rossi, 2020) that can strongly deviate from the Gaussian shape.

For MA-μPTV a different approach is taken with depth encoding based on the displacements of multiple images of the same particle, generated by different – in this case three – beam paths through a pinhole mask placed in the lens pupil. In the following, these particle image triplets will be referred to as *triplets*. For small volumes, the displacements b of the images of each triplet and therefore the size of the triplet varies nearly linearly with the change in depth along the viewing axis z. Using a simplified geometric analysis as provided in Willert & Gharib (1992) and Pereira & Gharib (2002), the depth sensitivity of such a microscopic setup, defined as $\partial b/\partial z$, can be predicted for different lens magnifications and pinhole separations. Fig. 2 compares sensitivities for two infinity corrected microscopic lenses in combination with a f_2=180 mm tube lens at a reference working distance of f_1=180/M and for a measurement volume of 0.5 mm depth. A nearly constant sensitivity can be achieved for a magnification of m=5 with sensitivities ranging from 73 to 83 pixel/mm for pinhole spacings between 6–8 and a pixel pitch of 13.5 μm. Assuming that

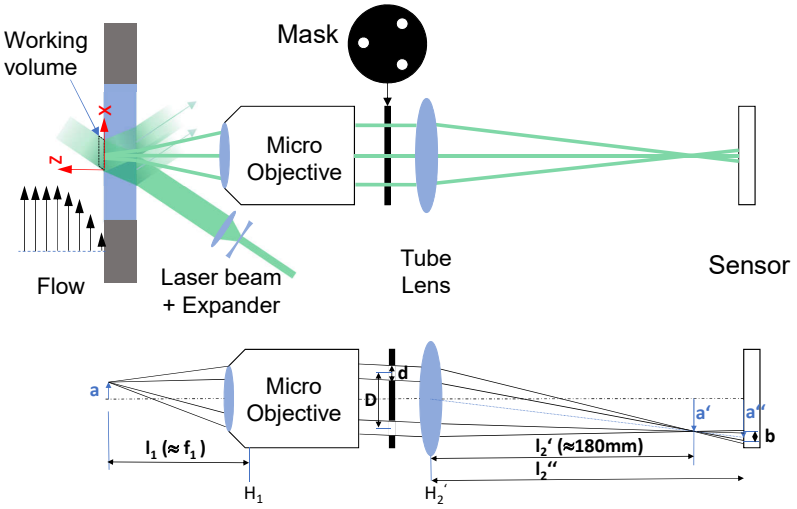

Figure 1. Optical arrangement (top) and simplified imaging geometry (bottom).

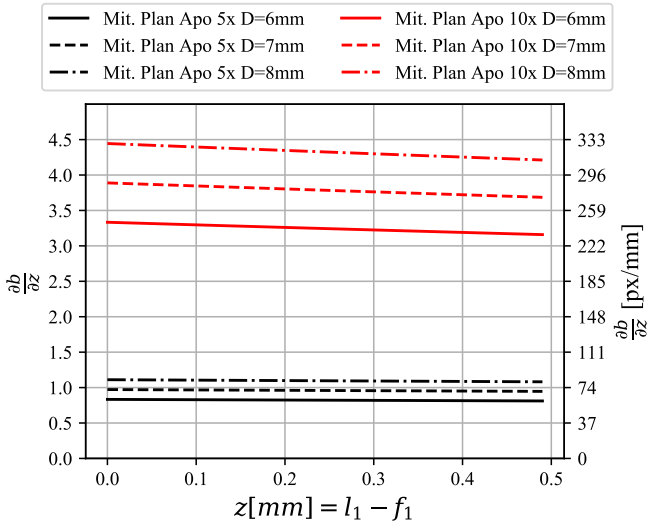

Figure 2. MA-µPTVsensitivity (image separation gradient) for two different infinity corrected microscope objectives in combination with a tube lens of $f = 180\,\mathrm{mm}$ and different separations of the pinhole mask D; The focal length f corresponds to that of the micro objective. Sensitivities in pixel/mm are provided at a pixel pitch of $13.5\ \mu\mathrm{m}$ (e.g. Vision Research v1840).

b can be detected with sub-pixel accuracy of 0.5 pixel for the given pixel pitch, a sensitivity of 83 pixel/mm would be sufficient to achieve an accuracy in z of 6 µm, which we found promising. Another aspect is that small pinhole diameters result in a reduced beam divergence compared to defocusing PTV, and thus to a lower particle image broadening over depth, albeit at proportionally reduced particle image intensities.

Since with MA-µPTV the particle images are always out of focus (defocused), sub-pixel position estimation has to deal with relatively broad particle images up to 6 pixels. At the same time limitations in the illumination intensity result in peak intensities that may just be slightly above the background noise. Therefore, a suitable weighting of image intensities in the neighborhood of the central intensity peak is essential for the accurate determination of the position in the measurement volume. With the intention of increasing position accuracies, triplet intensities are modeled by a geometrically constrained fit which will be assessed in comparison to a procedure, were center co-

ordinates of each of three particle images is fitted separately. To deal with non-Gaussian intensity distributions of strongly defocused particles, we introduce a weighting function for center determination based on a convolution of Gauss and Lorentz, also known as Voigt function, that more accurately reproduces the intensity variation on the flanks of the particle image.

Following a description of the optical setup, calibration images of microscopic dot grids are analysed to estimate the sensitivity and depth of field of the optical setup. Particle positions are determined by fitting the modeled intensities to each particle image triplet for which a detection and calibration procedure is described. The achievable depth-of-volume is assessed on the basis of actual particle image data. Finally, the MA-µPTV technique is applied in the TBL of a small wind tunnel at $\mathrm{Re}_\tau \approx 800$ to provide measurements in a wall-bounded volume of 1 mm depth. The obtained velocity statistics and shear rates are compared to high-speed, profile-PIV data (Willert et al., 2021) captured at a spatial resolution exceeding 3 pixel per viscous unit.

2. Windtunnel and flow conditioning

Feasibility tests were conducted in the turbulent boundary layer of a small scale wind tunnel operated in suction mode. The windtunnel has a 830 mm long test section with a square cross-section of internal width/height of $h = 76\,\mathrm{mm}$ (c.f. Fig. 3, right). Full-height glass windows provide optical access through the top and side windows. Optical access for MA-µPTV is provided through AR-coated N-BK7 glass windows of 8 mm thickness in the bottom wall. Flow conditioning upstream of the test section is provided by a settling chamber containing screens and straightening tubes followed by a rectangular nozzle of 10:1 area-contraction. Reproducible turbulent inlet flow conditions were ensured by tripping the laminar BL immediately at the nozzle exit by sharp-edged square teeth of side length $0.74\,\delta_0$ that are arranged regularly around the circumference at a pitch of $0.08\,h$. In order to homogenize the turbulence, an inlet section of $13\,h$ length was placed upstream of the transparent test section. Wall-shear measurements were conducted at $x/h = 14$ and $x/h = 20$. Reproducible flow conditions for both MA-µPTV and profile-PIV measurements were ensured by controlling the blower supply voltage and monitoring the pressure drop along the length of the channel. Measurements were conducted at mass flow rates corresponding to bulk Reynolds numbers of 30 500; 45 000 and 48 000 based on h and bulk velocity u_0. For these flow conditions, the smallest expected viscous unit is $l^+_{min} \approx 32$ µm at $x/h = 20$ corresponding to a friction velocity of $\mathrm{u}_{\tau,\mathrm{max}} \approx 0.49\,\mathrm{m/s}$.

3. Comparative profile-PIV measurements

To enable comparison of bin-averaged statistics obtained from MA-µPTV, comparative profile-PIV measurements were conducted at the same positions ($x/h = 14$ and $x/h = 20$). For PIV, the camera was equipped with a macro lens (Nikon, Nikkor Micro f105/4) and extension rings of 56 mm length which enabled a magnification near unity at an imaging ratios of 11.7 µm/pixel

such that one pixel roughly corresponds to one third of the smallest expected viscous unit, l^+_{min}. With frame rates set between 30–56 kHz the high-speed camera provided a reduced image size of 2048×128 pixel, which corresponded to an image area of 23.96×1.50 mm^2 thus enabling PIV profile measurements up to $h/3$ along the wall normal dimension z. At each position the light-sheet was introduced through the AR coated N-BK7 window on the bottom side by collimating the beam of the high-speed laser (Nanio Air 532-10-V-SP, Innolas Photonics) into a narrow, 2.5 mm wide light-sheet with a thickness of 250 µm ($8\,l^+_{min}$). Seeding consisted of paraffine aerosol created by a Laskin atomizer including an impactor which reduces the size fraction below 1 µm.

At both axial positions 8 bursts were recorded per test point each containing $N =$23 462 images corresponding to $N-1$ PIV image frames. To enhance particle image contrast and thereby improve the cross-correlation analysis, a mean intensity image, calculated from each burst's image sequence, was subtracted. The image data was analysed using a correlation-based, iterative, grid refining PIV processing scheme with final interrogation window sizes of 16×6 pixel ($5.9\,l^+_{min} \times 2.2\,l^+_{min}$ in x and z). PIV data validation was based on a normalized median filter with a threshold of 3.0 with which Validation rates of 99.9% were achieved. A further reduction of the noise in the velocity estimates was achieved by a multi-correlation processing scheme (cf. Willert et al., 2021) involving 3-5 successive frames. Particle images were evaluated using commercial software (PIVview 3.9, PIVTEC GmbH) and an in-house Python-based PIV package.

Near wall velocities and wall shear rates were determined from particle images by cross-correlating wall-parallel lines of pixels using one-dimensional dual- or triple frame algorithms as described by Willert (2015) and Willert et al. (2018). In streamwise direction, the length of the sample row corresponded to $47\,l^+_{min}$, in spanwise direction $\approx 8\,l^+_{min}$ (i.e. light-sheet thickness) and $0.37\,l^+_{min}$ in wall normal direction. Within this domain the near wall velocity was averaged to determine the wall shear.

4. Optical setup for MA-µPTV

The MA-µPTV optical setup consisted of an infinity corrected objective (Mitutoyo Plan Apo) in combination with a standard tube lens for microscopes of $f = 180$ mm as shown in Fig. 1. The thin mask consisted of a black anodized aluminum foil and was introduced into the nearly parallel optical path between the objective and the tube lens. The mask contained three pinholes precision-milled by CNC with a diameter d forming an equilateral triangle. The spacing between the pinholes D was maximized such that the apertures fall just inside the entrance pupil diameter D_{ep} which is determined by the back aperture of the objective.

The above mentioned microscope objective is available with various lens magnifications ranging from $m = 5$ up to $m = 10$ and feature both a relatively long working distance of 34 mm as well as a large entrance pupil of 11.2 mm. Based on Fig. 2 a sensitivity of approximately 80 pixel/mm was considered to be sufficient with the potential to achieve a depth accuracy of ± 6 µm or $\pm 0.2\,l^+_{min}$ (based on a dot detection accuracy of ± 0.5 pixel and a pixel pitch of 13.5 µm). Because seeding

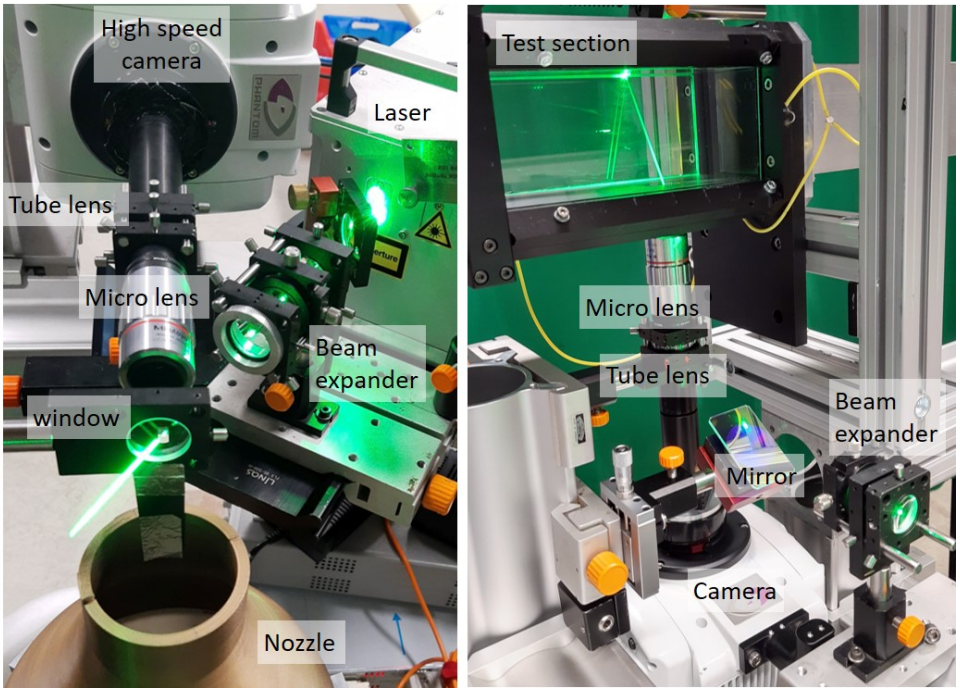

Figure 3. Photographs of setups for feasibility tests on a flow over a flat plate (left) and for wall-shear measurements in a small wind tunnel (right).

density is the limiting factor, a lens with increased magnification (i.e. $m = 10$) will not increase spatial resolution since the number of imaged particles would be reduced by roughly a factor of 4 in comparison to the $m = 5$ version. Therefore, a Mitutoyo 5× Plan Apo is used in the present setup.

At the given magnification the high-speed camera (Phantom v1840, Vision Research) provides a field of view (FOV) corresponding to 1.73×1.30 mm^2 at 640×480 pixels at a frame rate of 19 kHz and 1.73×0.82 mm^2 (640×302 pixels) at 30 kHz. The long side of the FOV was aligned with the main flow direction x in Fig. 1. To improve statistical convergence, 8 bursts were recorded per test point, with each burst containing 30 142 images at 19 kHz or 19 296 images at 30 kHz.

Tracer illumination was provided with a diode pumped pulsed solid state laser (Nanio Air 532-10-V-SP, Innolas Photonics), specified with an average power of up to 10 W at a pulse repetition rate of 40 kHz with a beam diameter of 0.8 mm. A beam expander is used to increase the beam diameter to roughly 2.0 mm to enable illumination of the entire measurement volume (cf. Fig. 3). The casing dimensions of the microscope objective limits the angle of incidence to $\approx 25^\circ$ to the z-axis, and is determined by the ratio of lens outer radius and the distance between measurement volume and lens. This also prevents direct back-reflections of the laser light from the window surface from being imaged by the sensor and thereby reduces the risk of damage.

Seeding is provided by the same tracers as used for particle image velocimetry (PIV). Preliminary tests on the flow over a small flat plate found that a pinhole diameter of $d = 2$ mm (f-number 18) capture sufficient back-scattered light at the intended frame rates, with triplets being imaged over

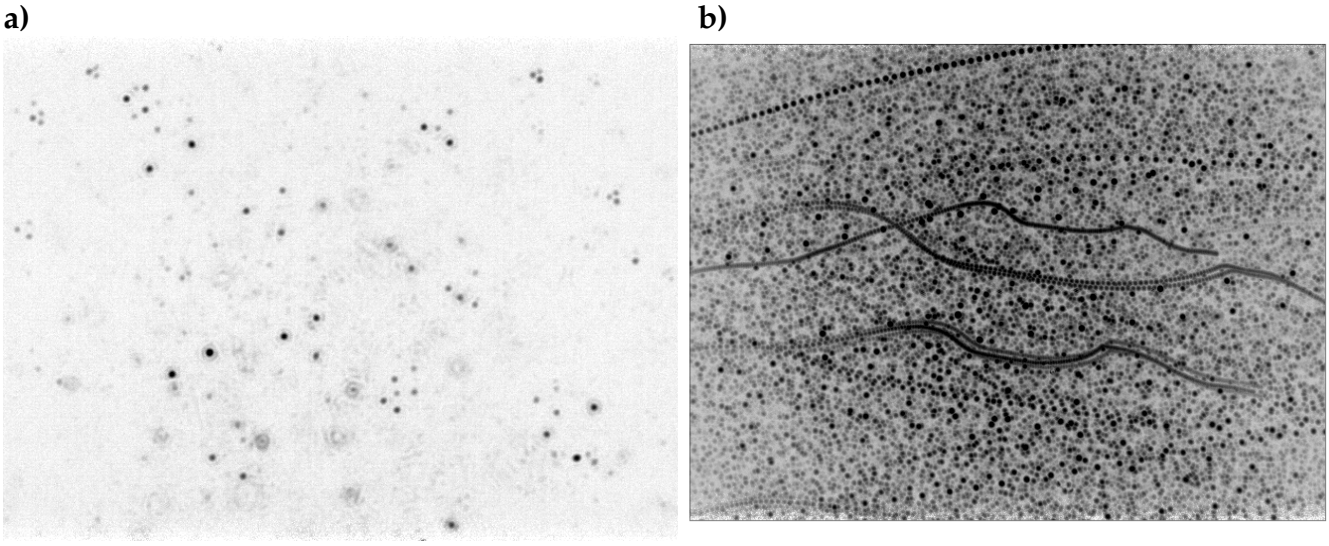

Figure 4. (a) MA-μPTVimage of 640×480 pixels (1.73×1.30 mm^2) recorded in a turbulent boundary layer at $\mathrm{Re}_\tau = 580$ (b) Composite image showing particle tracks obtained by overlaying 400 successive recordings acquired at 19 kHz (mean flow is from left to right).

a volume depth of about 1 mm.

Fig. 4a) exemplarily shows a MA-μPTV image at Re_0=45 000, indicating that triplets images were sparsely populated in the present data. Between the highest and lowest Reynolds numbers, the triplet image densities varied between 0.0001–0.0002ppp. Fig. 4b visualizes particle tracks from the near wall flow by overlaying 400 MA-μPTV images at 19 kHz at $x/h = 20$. Considerable transverse motions are clearly for particles very close to the wall (smallest triplets).

5. Geometric calibration

For MA-μPTV a geometric calibration is required to provide parameters defining the orientation of the triplets (i.e. the search direction to find corresponding images of the same particle), the sensitivity (i.e. the separation gradient) and the magnification along with the variation of these parameters across the field of view.

For each measurement location the calibration procedure was conducted using a lithographically manufactured dot grid on a 3 mm thick lime glass substrate with the glass surface aligned parallel with the bottom wall of the windtunnel. The dot diameter was 5 μm at an equilateral spacing of 150 μm along x and y. The glass plate was back-lit with a green LED and was traversed by a small motorized translation stage to record image-to-object point correspondences across the depth of volume. A sample image is provided in Fig. 5. The translation stage was driven by a piezo motor in closed loop operation with position feedback by a linear encoder (accuracy of 0.2 μm).

Dot image positions were initially located in segmented regions of each calibration image by a simple center of mass approach, with segmentation based on template matching with a circular

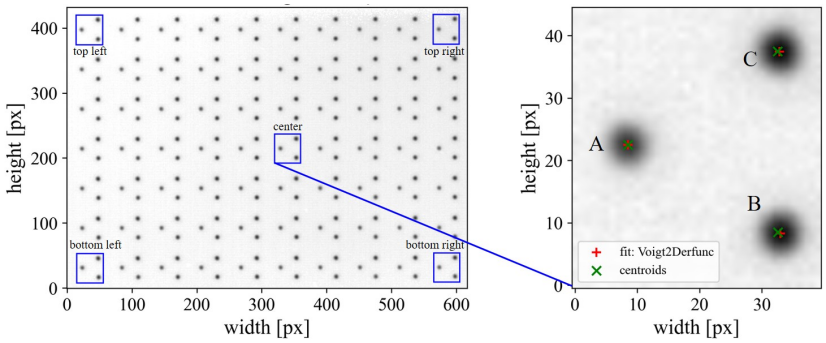

Figure 5. MA-µPTV calibration image of a microlithographically produced dot pattern on glass of dot diameters of 5 µm and 150 µm square grid spacing; the inset shows the magnified center triplet image with coordinates determined using centroids and a particle image fit on the basis of a radial Voigt profile.

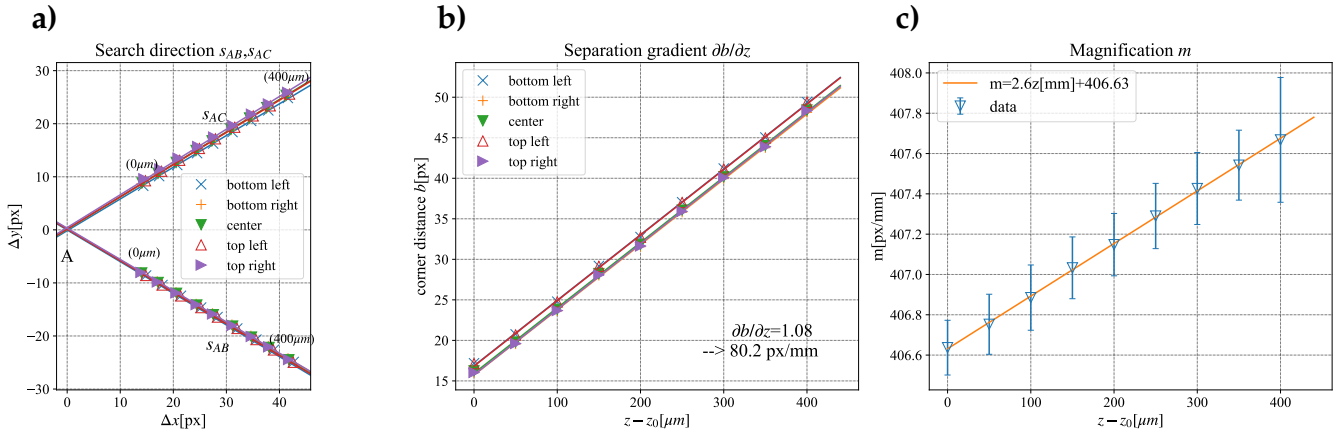

Figure 6. MA-µPTV geometric calibration parameters for different image regions as indicated in Fig. 5: a) orientation of triplet images and search direction with plate positions provided in brackets; b) corner distance versus focal distance; c) magnification versus focal distance.

template of 4 pixels in diameter. In a second step, the dot positions were refined by minimising the squared difference between image intensities and a particle image model over a template of up to 16×16 pixel. The spot intensities were modeled using a radial Voigt profile, which represents the convolution integral of a Lorentzian and Gaussian and provides more accurate position estimates compared to a Gaussian. The Gaussian fit was found not to converge from a focal distance of $z \geq 550$ µm. For the remaining planes, where the Gaussian fit succeeded, the standard deviation of grid spacing is 0.02−0.08 pixel for all calibration points across the field of view. By applying the circular Voigt profile the standard deviation reduces down to 0.02−0.03 pixel for planes below a focal distance of $z \leq 600$ µm and increases toward 0.05 pixel for $600 < z \leq 650$ µm.

Fig. 6 shows calibration results for triplets near the image corners and in the image center as highlighted in Fig. 5,left. Fig. 6a) indicates a slight variation of the search direction $s_{AB} = \Delta y_{AC}/\Delta x_{AC}$ over the field of view and is especially visible for the bottom left and top right image corners in Fig. 5. Fig. 6b indicates a rather constant slope of the separation gradients $\partial b_{AB}/\partial z$ and $\partial b_{AC}/\partial z$, but exhibits a varying offset between $16 - 17$ pixels at $z = 0$ (corresponding to an offset of about $z_0 = 206$ µm to the focal point). There are two reasons for this: first, the position at which the

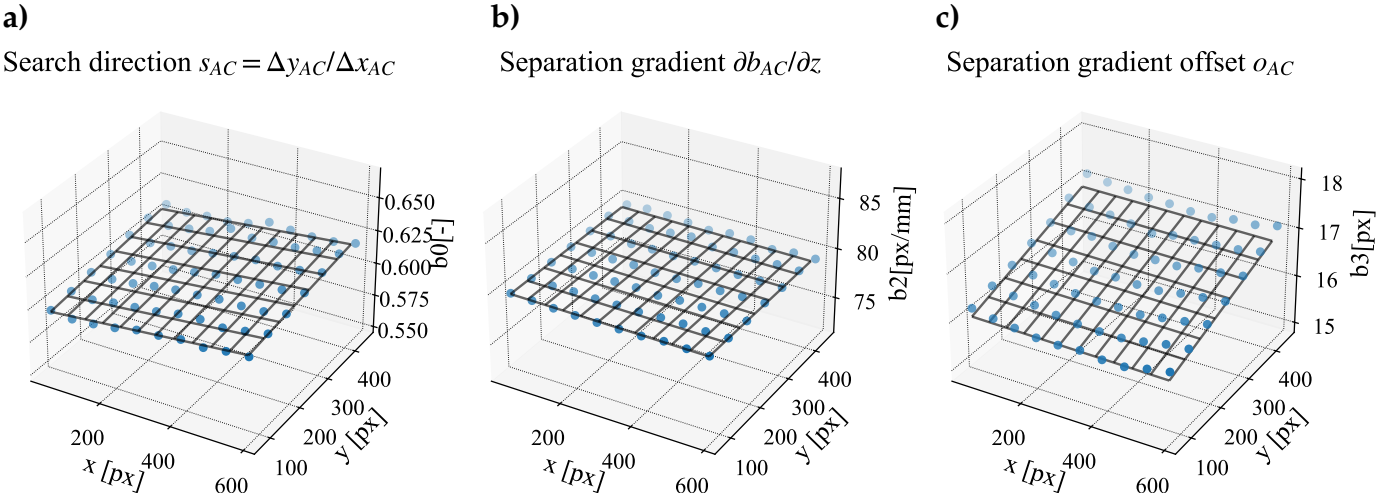

Figure 7. Variations of calibration parameters over the field of view and corresponding linear parameter fits.

triplets converge to a point was set to be within the glass to have clearly defined triplets in the wall-bounded measurement volume, and second, there is always a minor offset between wall and calibration target. The final offset to the wall is determined during evaluation of the wall gradient and is subtracted during postprocessing.

The variations of the separation gradient and z-offset over the FOV as visible in Fig. 6b probably have their origin in the wall/calibration plate not being co-planar with the camera sensor plane. To compensate for this effect, a plane was fitted through the spatially varying calibration parameters used later to interpolate separation gradient and search direction at each particle image position. Fig. 7 compares calibration parameter for one of three sides of the triangle which exhibits the largest variations over the image plane (side $A - C$ in Fig. 5 and Fig. 6). Search direction and separation gradient are well approximated by the planar fit with a maximum residuum of less than 1% of mean. The offset o_{AC} exhibits a maximum deviation from the plane fit of 0.17 pixel (1.1% of mean offset) corresponding to a bias in the z position of up to 2 µm ($0.064\, l^{+}_{min}$) over the field of view, which is considered acceptable.

Finally, variations of the magnification within the measurement volume have to be taken into account as indicated in Fig. 6c. Pincushion or barrel distortion effects could not be detected with the optical configuration used (Apo-planar objective + N-BK7 window), as indicated by the small deviation from the mean magnification per calibration plane of 0.5% maximum.

One behavior that is strange at first sight is that in Fig. 6c the magnification increases with the wall-distance z which is contradictory to imaging with a single convex lens where the magnification always decreases with increasing object distance. The two-stage imaging in MA-µPTV was identified as the reason for this behaviour, where the total magnification between object an sensor plane becomes $m = m_1\, l''_2/l'_2$ (cf. Fig. 1). For small changes in the object distance Δl_1, it can be shown, that the image distance $\Delta l'_2$ varies greatly according to $\Delta l'_2 = -m_1^2\, \Delta l_1$ with m_1 corresponding to the lens magnification ($m \approx 5$). In other words, if the distance of the particle to the

microscope objective increases slightly, the difference in the image distance decreases by a factor of 25. On the other hand, m_1 decreases only slightly with increasing wall distance. Both results in a decrease in l_2' while the distance of the particle to the optical axis a' remains approximately the same and thus, at a fixed sensor distance of l_2'' the effective m increases slightly with z for $z << l_1$. According to Fig. 6c and a measurement volume of 1 mm depth, m would increase by 0.6%. This is taken into account when particle displacements in pixel are converted to velocity using a linear fit of $m(z)$.

6. Triplet image detection and fitting

To accurately determine the 3d position of a particle, a geometrically constrained triplet image model was implemented that, starting from one corner of the triangle, only accepts corresponding image positions on straight lines starting from this point. Since the orientation of the triangle-shaped triple images is known very precisely from the calibration, the idea here is to only allow image positions that lie on the vertices of this triangle for images that belong to the same particle. This way initial corner and particle positions are improved by minimising the squared difference between triplet image intensities and model intensities within a certain region around each spot.

For the implementation of this detection scheme some peculiarities of triplet images have to be taken into account. As evident in the sample recording Fig. 4a triplets at a given wall distance can have very different brightness levels. The reason might be the different scattering behavior of tracer particles of different sizes as well as different radiances within the oblique incident laser beam. In addition, the vertices of a single triplet may also vary in brightness and width, which might be caused by the inhomogeneous scattering behavior of the liquid droplets coupled with the coherent nature of the laser light source. Finally, the holes in the mask, which is made of a thin anodized aluminum foil, may have slightly different diameters due to the manufacturing process.

Therefore, for least squares fitting images intensities of each spot are weighted differently as follows:

$$\begin{aligned} I_T(x,y) &= a_A W(r_A(x,y)) + a_B W(r_B(x,y)) + a_C W(r_C(x,y)) + off \\ r_A(x,y) &= \sqrt{(x-x_c)^2 + (y-y_c)^2)} \\ r_B(x,y) &= \sqrt{(x-x_c-\Delta x_{AB})^2 + (y-y_c-s_{AB}\Delta x_{AB})^2} \\ r_C(x,y) &= \sqrt{(x-x_c-\Delta x_{AC})^2 + (y-y_c-s_{AC}\Delta x_{AC})^2} \end{aligned} \tag{1}$$

Here, $W(r_A)$,$W(r_B)$ and $W(r_C)$ are the intensity weights based on one-dimensional circular Gaussian and/or Lorentzian distributions (Voigt-like) for which the widths σ and γ are evaluated by calibration as will be described further below. Fitted parameters are the center coordinates x_c, y_c of corner A the spacings Δx_{AB} and Δx_{AC} between A,B and A,C along x as well as intensity variations between the triple images a_A,a_B and a_C and a common offset off.

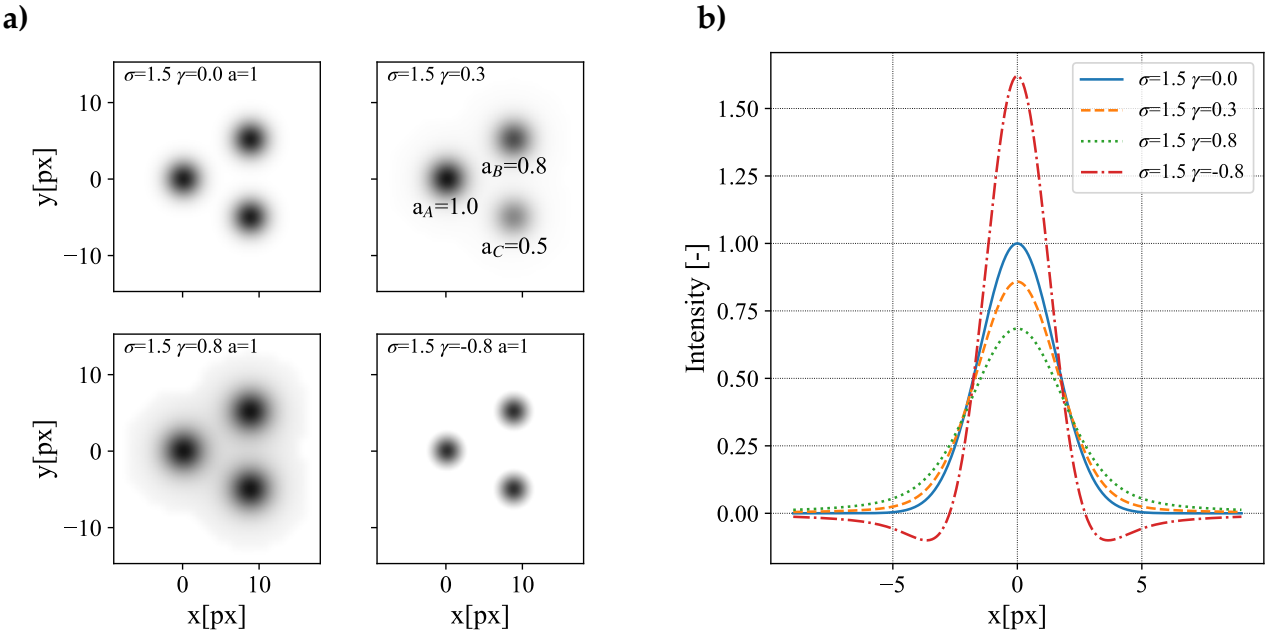

Figure 8. a) Samples of image templates used for least squares optimization of the particle position according to Eq. (1) (b) Weighting function that bases on the Voigt profile according to Eq. (4)

Parameters are obtained by a least squares optimization that tries to minimize the cost function which is the sum of squared differences between image and model intensities over the pixels $(x, y)_i$ in the neighborhood of each corner A, B, C. To allow overlap of the triplets and reduce computational effort, the cost function is evaluated only within a certain radius around the initial positions of each triple image peak, typically within a radius between 4−7 pixels. For least squares fitting the Levenberg-Marquardt algorithm is used as implemented in LMFIT for python (Newville et al., 2014).

Fig. 8 provides samples of triplet weighting functions for different widths and heights.

The particle's z position is evaluated by dividing the triangle's side lengths by the separation gradient, where the offset o_z (in pixels) is used to compensate for possible deviations from sensor-wall parallelism as obtained from geometric calibration:

$$\begin{aligned} z_{AB} &= (\sqrt{1+s_{AB}^2}\,\Delta x_{AB} - o_{AB})\,(\partial b_{AB}/\partial z)^{-1} \\ z_{AC} &= (\sqrt{1+s_{AC}^2}\,\Delta x_{AC} - o_{AC})\,(\partial b_{AC}/\partial z)^{-1} \\ z &= (z_{AB} + z_{AC})/2 \end{aligned} \tag{2}$$

The disparity between z positions from each triangle leg $\epsilon_z = 0.5\,|z_{AB} - z_{AC}|$ is a measure of the accuracy of the particle's position. Finally the particle's lateral position in $(x, y)_p$ is obtained by the mean of the center coordinates of the three dots of each triplet.

As described in the following section, calibration of the width of the weighting function from triplets revealed that for particle images far from the focus, in this case more than 500 µm, the

intensity deviates from a Gaussian curve mainly at the flanks (cf. Fig. 9). In order to account for possible non-Gaussian distributions the weights of the triplet image model are calculated either by a Gaussian or alternatively by the convolution of a Gaussian and a Lorentzian which is determined by the so-called Voigt profile V:

$$\begin{aligned} V(r;\sigma,\gamma) &= (G * L)(r) = \int_{-\infty}^{+\infty} G(r)L(r-r')dr' \\ G(r;\sigma) &= \frac{e^{-r^2/(2\sigma^2)}}{\sigma\sqrt{2\pi}} \\ L(r;\gamma) &= \frac{\gamma}{\pi(r^2+\gamma^2)} \\ r &= \sqrt{(x-x_c)^2+(y-y_c)^2} \end{aligned} \tag{3}$$

Here, $G(r,\sigma)$ and $L(r,\gamma)$ are the centered Gaussian and Lorentzian profiles. The convolution integral V can be evaluated by the real part of the complex error function $w(Z)$

$$\begin{aligned} V(r,\sigma,\gamma) &= \frac{\Re(w(Z))}{\sigma\sqrt{2\pi}} \\ Z &= \frac{r+i\gamma}{\sigma\sqrt{2}} \end{aligned} \tag{4}$$

According to numerical assessments by Schreier (2019) Weideman's rational approximation by 32 coefficients (Weideman, 1994) was used to implement the complex error function. To reduce the computational effort of fitting, parameter derivatives (i.e. Jacobian) are specified analytically for both Gaussian or Voigt-like weighting functions.

Fig. 8b shows examples of a Voigt profile for different widths, where the full-width at half maximum (FWHM) of the Gaussian is $g_G = 2\sigma\sqrt{2ln(2)}$ and $g_L = 2\gamma$ for the Lorentzian.

Calibration of teh particle image width on the basis of Voigt profiles showed, that negative values for γ can also occur close to the focus, which result in a weighting for which the slopes are steeper than for a the pure Gaussian function in addition to a negative side slope in the weighting function (as also demonstrated in Fig. 8).

7. Calibration of particle image width

Prior to fitting the triplet templates according to Eq. (1), the width of the weighting functions was evaluated. The processing, occasionally also referred to as *calibration of the point spread function (PSF)* will be described next.

Contrast enhancement of the raw image data was performed first by dividing each image by the average image of each record. Then bright spots in each image were identified using correlation-based thresholding (template matching) by convolution with a template of 8×8 pixels that contains a circular mask of a diameter of 6 pixels. Potential particle images were identified for regions exceeding a given threshold of the normalized cross-correlation coefficient. In comparison

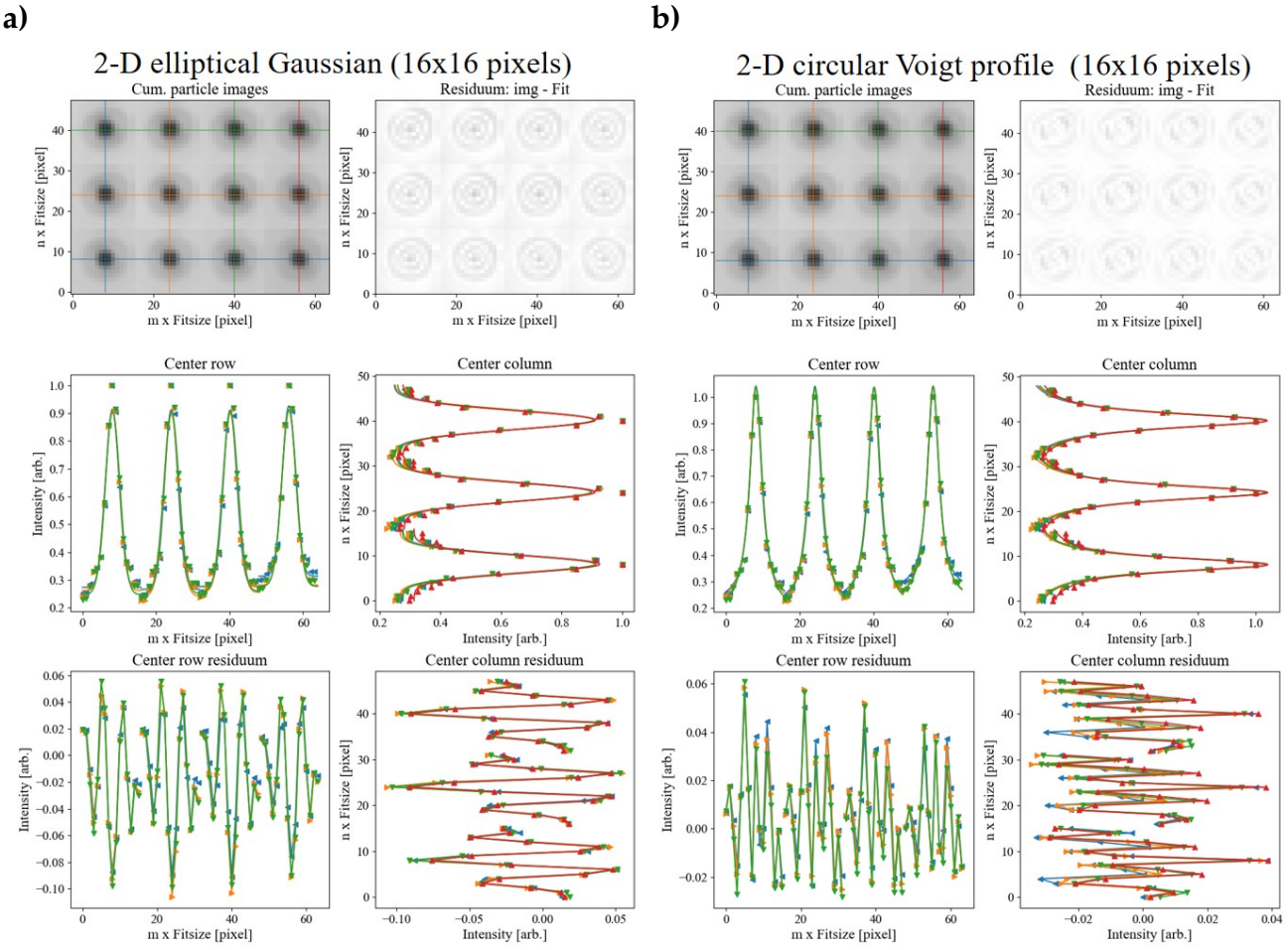

Figure 9. Cumulated defocused triple images (one of three corners) at 3×4 ($m \times n$) different regions of the field of view as used for PSF calibration at a focal distance between 500 µm $\leq z < 600$ µm (fit size 16×16 pixels): a) elliptical Gaussian (cf. Schanz et al. (2013)); b) circular Voigt profile; *Top* cumulated particle images and absolute fit residuum; *Middle* data and fit from center rows and columns; *Bottom* fit residuum from center rows and columns; Color of lines and symbols correspond to the position as indicated in the cumulated image top left.

to intensity-based thresholding, the correlation-based particle image detection was found to be more robust compared with regard to separation of triplets. Image regions segmented in this way were filtered to exclude regions covering an area smaller than a certain threshold, i.e. 2 pixels, since these regions were primarily associated with noise. To find triplet candidates, the neighborhood of each region center was searched for adjacent region centers with displacements corresponding to the corners of the equilateral triangle plus a tolerance ϵ using the parameters obtained from the geometric calibration. The triplet candidates were then validated based on the difference of the side length (should be near zero if the triangle is equilateral).

For PSF estimation, each image of the triplet was fitted separately to a Voigt profile. In order to estimate the mean width from noisy particle images, centered particle images are accumulated separately for each corner (A, B, C) in $m \times n \times o$ adjacent spatial bins of $400 \times 400 \times 100$ µm^3 size along x, y, z.

It was found that for a focal distance range of $600-700\,\mu m$, the Gauss fit partially failed to converge. For the cumulated bin averages that are near to the focus, the residuals for the Gauss fit (i.e. (sum of absolute differences between data and model) were sometimes a factor of 1.8 larger than for the Voigt fit. An elliptic Gaussian function (Schanz et al., 2013) was also tested, but it brought little improvement compared to a the circular symmetric Gaussian.

For both weighting functions (elliptical Gaussian and circular symmetric Voigt profile) the different behaviour is demonstrated in Fig. 9 as evaluated from center positions in 19 296 images that lay in a focal distance between $500\ \mu m \leq z < 600\ \mu m$. The top row shows both the cumulated centered particle image intensities for one corner of the triangle and the corresponding residual image after fitting and subtracting image intensities obtained from the corresponding weighting function. In general, for positions with a large focal distance, the diameter of the particle images exceed 6 pixel (FWHM). For the elliptical Gaussian, the residual image reveals differences at the center and at the image tails, visible through concentric rings. The middle row in Fig. 9 shows an underestimation of center intensities for the Gauss fit with fit residuals on the edges more than $2\times$ larger compared to the Voigt profile. The reason is probably, that in addition to a pure diffraction-limited ideal PSF (i.e. Airy disc), geometric aberrations of the lens and window along with internal reflections on the window, become increasingly important at large distances from the focus and probably produce a halo that leads to a redistribution of intensity from the center toward the edges.

Depending on the weighting function, the widths (γ, σ) are fitted linearly at each bin position to obtain parameter fits that are used to interpolate the particle image width at each 3d particle position. For the Gaussian weighting, the particle image width σ is extrapolated linearly if the fit based on cumulated centered particle images failed.

The procedure of PSF calibration was repeated, with the image width specified by the parameter fit, until the fitted particle image widths/residuals converge.

8. Processing of triple images, tracking procedure and bin averaging

8.1. Triplet detection

Based on the parameters from the PSF calibration, the particle image positions are re-evaluated by minimizing the sum of squared differences between image and model intensities in the neighborhood of each initial corner position using the triple image model (cf. Eq. (1)). Prior to the fitting, the initial positions of the triplets are determined by the image enhancement described in the previous section. Fig. 10a shows a sample image processed as described above. The centers of the particle images resulting from the triplet matching are indicated by red circles, with the wall distance in μm. In the corresponding residual image in Fig. 10b the remaining triples are barely distinguishable from the speckled background intensities. The blue circles mark a highly defocused triplet where the particle images are too distorted and initial corner detection with subsequent matching fails. At this point it is difficult to visually detect further possible triplets in the

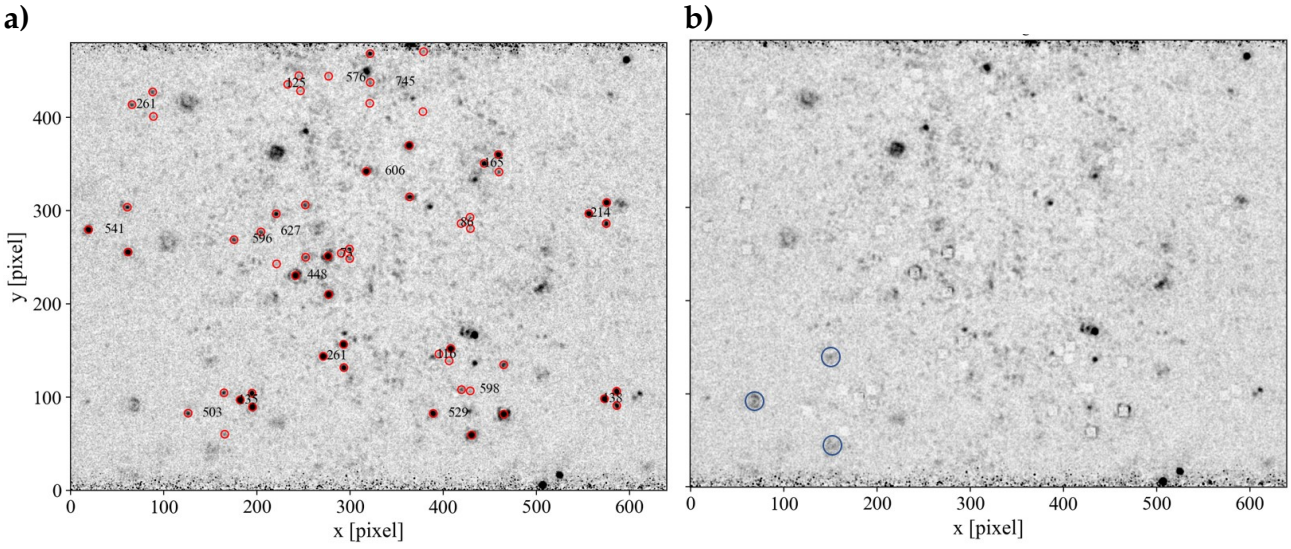

Figure 10. a) MA-µPTVsample image at $x = 14h$ with fitted triplets indicated by red circles; numbers correspond to the wall distance µm, b) Corresponding residual image with fitted intensities subtracted; Blue circles indicate where a triplet is too far from focus to be detected.

residual image, so it can be assumed that the intended processing is efficient at finding triplets with intensities above the cameras noise level.

8.2. Track reconstruction

Lagrangian particle tracks were initialized with up to four image frames using classical techniques as described by Malik et al. (1993) and Ouellette et al. (2006). Starting from the first image, the nearest neighbors in the following image are searched in a domain constrained by a given range of the wall distance (20% of Δz) with respect to the neighboring time steps, which is considered an appropriate criterion for a wall-bounded flow. Initialization of the predictors towards the second frame on the basis of neighboring tracks in the first frame (cf. Malik et al., 1993) was discarded here because, due to high shear rates, only neighbors with approximately equal wall distance and only within a search radius of the Kolmogorov length scale of O(60 µm) can be considered, which rarely occur at the present low particle image density. On the other hand, the same particle may occasionally disappear and then reappear in the following frame due to varying intensity levels (speckle). Therefore, the third frame is also included in the nearest neighbor search if no candidate is found in the second frame. Using the displacements between possible particle matches as predictors, candidates are targeted in the third frame within a constant maximum search radius. In the present case, the maximum search radius was set to a constant value $r_{max} = u'_{max}\,\Delta t/M$, where u'_{max} was estimated according to the near-wall maximum of the streamwise velocity fluctuation u' in a zero pressure gradient turbulent boundary layer (ZPG-TBL) ($u'_{max} \approx \sqrt{8}\mathrm{u}_{\tau,\mathrm{max}}$). If no suitable candidate is found, the fourth frame is also included using twice the previous displacements. From candidates that are linked in three frames, the track with the smallest change in velocity is selected (e.g. minimum acceleration criterion). To continue tracks from length three, the predicted

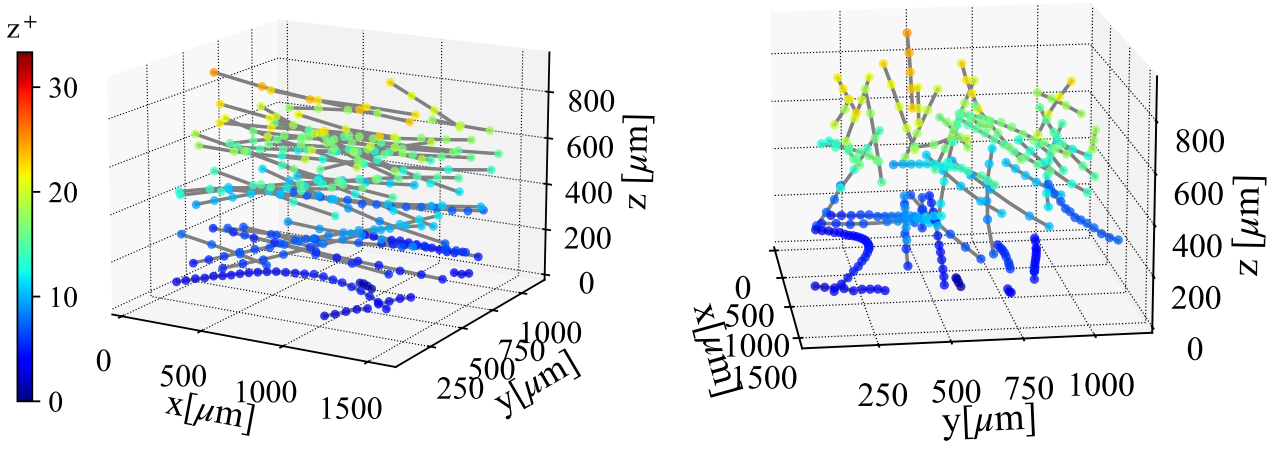

Figure 11. The first 50 tracks at Re_0=45 000, Re_τ=580, $l^+ = 36$ µm recorded at a frame rate of 19 kfps. In total 187 183 tracks could be retrieved from $8 \times 19\,296$ images under these conditions.

displacement toward following frames base on the velocity difference to the predecessor plus the displacement extrapolated from the acceleration in the previous two frames. Alternatively, a predictor was tested that bases on the tangent of a cubic-b-spline fitted through the last four track members. After forward tracking is performed over a set of frames, shortest tracks that consist of only three members are removed based on an acceleration threshold of 2%. With the spurious tracks removed, the entire tracking procedure is repeated for the remaining unlinked particles in backward time association, followed by removal of short tracks. A sample result of this tracking procedure is shown in Fig. 11 indicating several tracks inside the viscous sub layer.

8.3. Post-processing

To allow comparison with flow statistics obtained with PIV, a bin-averaging scheme with bin-heights of 16 µm ($\leq 0.5 l^+_{min}$) in wall normal direction was used and results in 5 000 to 40 000 entries depending on the wall distance (cf. Fig. 12 and operation conditions). Therefore, the velocity of each linked particle is either interpolated from the first derivative of cubic b-splines over all track members (for track length > 3) or estimated from particle displacements, if the track has three members only. The assignment into the equally spaced bins is performed using bilinear weighting.

Bin averaging was also used to evaluate dependence of particle detection on the wall distance. As can be seen in Fig. 12, the number of particles detected decreases approximately linearly with the wall distance z. This decrease in particle counts is most likely due to the restricted depth of focus of the method, where particles at greater distances from the focus have proportionally decreased,making them less detectable (see Fig. 10b). In addition, significantly increased velocities at higher wall distances result in decreased track lengths. Similarly the increased degree of turbulence in the buffer layer leads to a decreased number of linked particles. An assessment of this

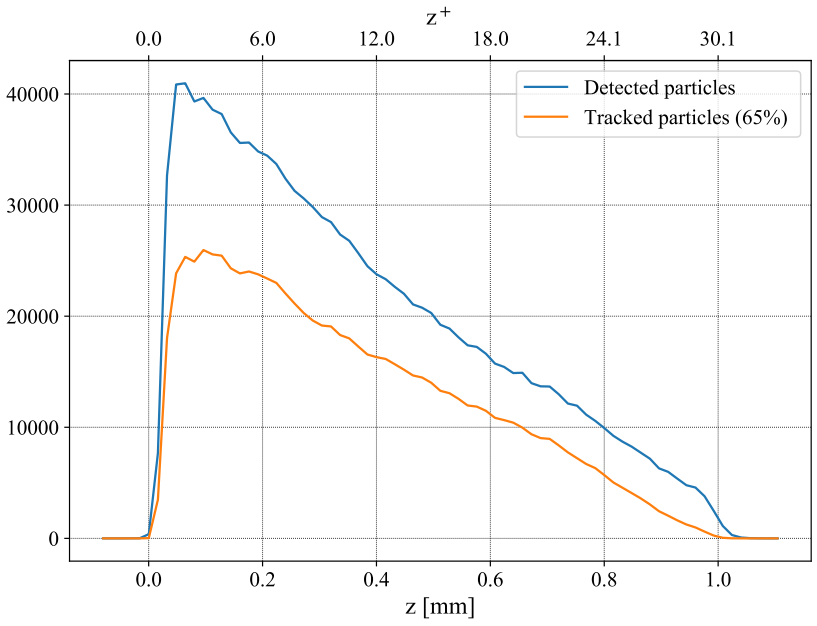

Figure 12. Bin-averages of detected particles (in total 1.3×10^6) and of particles assigned to tracks at Re_0=48 000, Re_τ=600 for in total $8 \times 30\,142$ frames and a field of view of 1.73×0.82 mm^2 (640×302 pixels).

underestimation and its influence on the turbulence statistics is subject of the following section.

9. Results

Fig. 13 compares the mean near wall velocities at $x/h = 14$ as obtained from cross-correlation of wall-parallel pixel rows (corrR-PIV) and from MA-µPTV. The mean velocity gradient is evaluated by a linear least squares fit. To ensure values inside the linear range only wall distances up to $4\,l^+$ were considered (faded symbols indicate unused data points). Friction velocities and viscous units obtained by this method are provided in the plot legend. Also shown in the plot legend is the gradient fit standard error (s.e.) on the linear least square fit according to Hutchins & Choi (2002). The horizontal error bars indicate the uncertainty in velocity taking into account the measurement uncertainty of the differential pressure transducer of 0.5 Pa. This transducer was intended to ensure re-producible flow velocities for non-simultaneous PIV and MA-µPTV measurements. Error analysis of the pressure related bulk velocity is based on assumption of a fully turbulent channel flow and a d'Arcy friction factor of a square duct (cf. Jones, 1976). For the MA-µPTV data, vertical error bars represent the mean disparity of the depth reconstruction based on Eq. (2). The mean wall gradients obtained from MA-µPTV and corrR-PIV are in good agreement within the uncertainty of the differential pressure. Both corrR-PIV and MA-µPTV (Gaussian triplet fit, label *Tr. Gauss*) exhibit quite similar fitting errors of the wall gradient except for the largest Re_0 where the error for MA-µPTV increases slightly but is still below 1%. For the Voigt-type particle fit (label *Tr. errFun*) the gradient fitting error further increases to 1.2% thus indicating that a pure Gaussian representation of image intensities is sufficient in the near wall region. One way to implement this by an

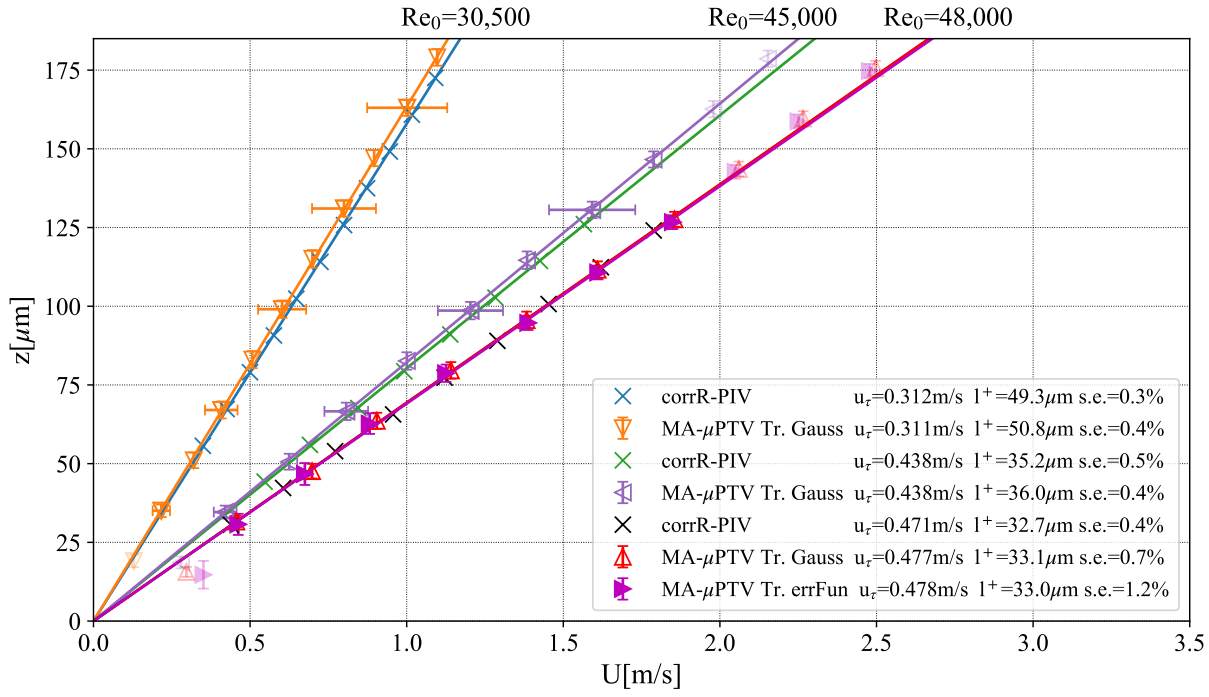

Figure 13. Mean wall gradient at $x/h = 14$; The horizontal error bars correspond to the uncertainty of the bulk velocity due to an error of 0.5 Pa in the differential pressure measurement. Vertical error bars indicate the mean z-disparity at each point; Lines indicate the fit, Fading points are not fitted.

universal Voigt-type fit would be to set γ to zero up to a certain focal distance (cf. Fig. 8b). Table 1 summarizes linear fitting errors as well as the friction velocities and viscous units for various free stream conditions and for both measurement locations.

The streamwise probability density distribution of the wall shear rates at Re_0=48 000 and $x = 14h$ is provided in Fig. 14a) and indicates a standard deviation of $\sigma(\tau_x')/\tau_x = 0.421$ which is consistent with a correlation proposed by (Örlü & Schlatter, 2011) yielding $\sigma(\tau_x')/\tau_x = 0.298 + 0.018\, ln(\mathrm{Re}_\tau) = 0.413$. Kurtosis and flatness correspond to values reported in other ZPG-TBL experiments (e.g. Willert et al., 2018). The spanwise distribution (cf. Fig. 14b) exhibits a standard deviation of $\sigma(\tau_y')/\tau_x = 0.209$ which is significantly below the correlation $\sigma(\tau_y')/\tau_x = 0.164 + 0.018\, ln(\mathrm{Re}_\tau) = 0.279$ as proposed by Diaz-Daniel et al. (2017) for ZPG-TBL. This is thought to be caused by the square cross-section of the wind tunnel which dampens spanwise fluctuations.

Mean velocity profiles for several free stream conditions are provided in Fig. 15, normalized by the corresponding viscous unit and friction velocity. Profile-PIV indicates a clear logarithmic region as expected for this type of flow. The mean streamwise velocity u agrees well with the DNS of a turbulent channel flow at $\mathrm{Re}_\tau = 1000$ and $\mathrm{Re}_0 = 20\,000$ by Lee & Moser (2015). Depending on the measurement location the velocity deviates from the log-law beyond $z^+ = 200$ at $x/h = 14$ and from $z^+ = 300$ at $x/h = 20$ indicating that the turbulent channel flow is not yet fully converged. At both measurement positions the velocity profile resembles that of a ZPG-TBL.

For the present setup MA-µPTV can provide velocity measurements up to the beginning of the

Table 1. Linear fitting error (cf. Hutchins & Choi, 2002) of the wall gradient and derived friction velocity and viscous units for different free stream conditions as obtained from cross-correlation of wall-parallel pixel rows (corrR-PIV) and from MA-µPTV with 3d positions computed from a Gaussian triplet fit Eq. (1).

Re_0	x/h	err_τ [%]		u_τ[m/s]		l^+[µm]	
		corrR-PIV	MA-µPTV	corrR-PIV	MA-µPTV	corrR-PIV	MA-µPTV
30 500	14	0.3	0.4	0.312	0.311	49.3	50.8
45 000	14	0.5	0.4	0.438	0.438	35.2	36.0
48 000	14	0.4	0.7	0.471	0.477	32.7	33.1
30 500	20	0.2	0.6	0.320	0.319	48.1	49.5
45 000	20	0.8	1.0	0.455	0.454	33.8	34.8
48 000	20	1.0	0.5	0.488	0.482	31.6	32.8

logarithmic region or up to a wall distance of about 1 mm (i.e. 30 l^+ at the highest Reynolds number). The velocities measured in this way agree very well with both the profile-PIV data and the DNS data. Measurements beyond this wall distance are not possible for the present optical configuration ($m = 5$, $d = 2$, $D = 8.2$), which is also indicated by the rapidly decreasing velocities (fading colors) where only few slow particles can be tracked reliably.

Fig. 16a show profiles of the velocity variances $\langle u'u' \rangle$, $\langle v'v' \rangle$, $\langle w'w' \rangle$ and covariances $\langle u'w' \rangle$ at $Re_0 = 48\,000$, $x = 14\,h$, $l^+ = 33$ µm. Again DNS of a channel flow (Lee & Moser, 2015) and of a ZPG-TBL (Schlatter & Örlü, 2010) are shown for reference. For $z^+ > 10$ ($l^+ = 33$ µm), the limitations in focal depth of MA-µPTV result in less converged second order statistics since the number of samples contributing to the bin-averages drop from $N = 17\,000$ at $z^+ > 10$ to $N < 3\,000$ at $z^+ = 27$. Nonetheless, the "inner peak" of the streamwise velocity fluctuation $\langle u'u' \rangle$ is well resolved by MA-µPTV and follows the DNS data up to $z^+ = 28$. The same is valid for $\langle v'v' \rangle$ and $\langle u'w' \rangle$. The streamwise variance $\langle u'u' \rangle$ agrees well between profile-PIV and MA-µPTV up to the buffer layer while the "inner peak" is slightly smaller for profile-PIV data. The limited number of MA-µPTV samples along with uncertainties in u_τ prevent a quantification of the observed differences between the two measurement techniques.

When comparing the present data with DNS of a channel flow, it must also be taken into account that at the points of measurement, however, the turbulent flow in the square channel has not yet fully converged to a turbulent channel flow with the center portion of the flow beyond $z^+ = 700$ essentially devoid of turbulence. While the measured profiles agree well with DNS of the channel flow up to $z^+ = 30$ at increasing wall distances, the quantities $\langle u'w' \rangle$ and $\langle w'w' \rangle$ are more in agreement with DNS of a ZPG-TBL.

In Fig. 16a various profiles are added as evaluated with MA-µPTV using a Gaussian ("Tr. Gauss" Eq. (1)) and a Voigt-type triplet fit ("Tr. errFun" Eq. (1),Eq. (4)) as well as an evaluation where the depth position is obtained after improving each initial triplet corner separately using Gaussian fits that are not geometrically constrained ("Si. Gauss"). The profiles of these three variants are almost

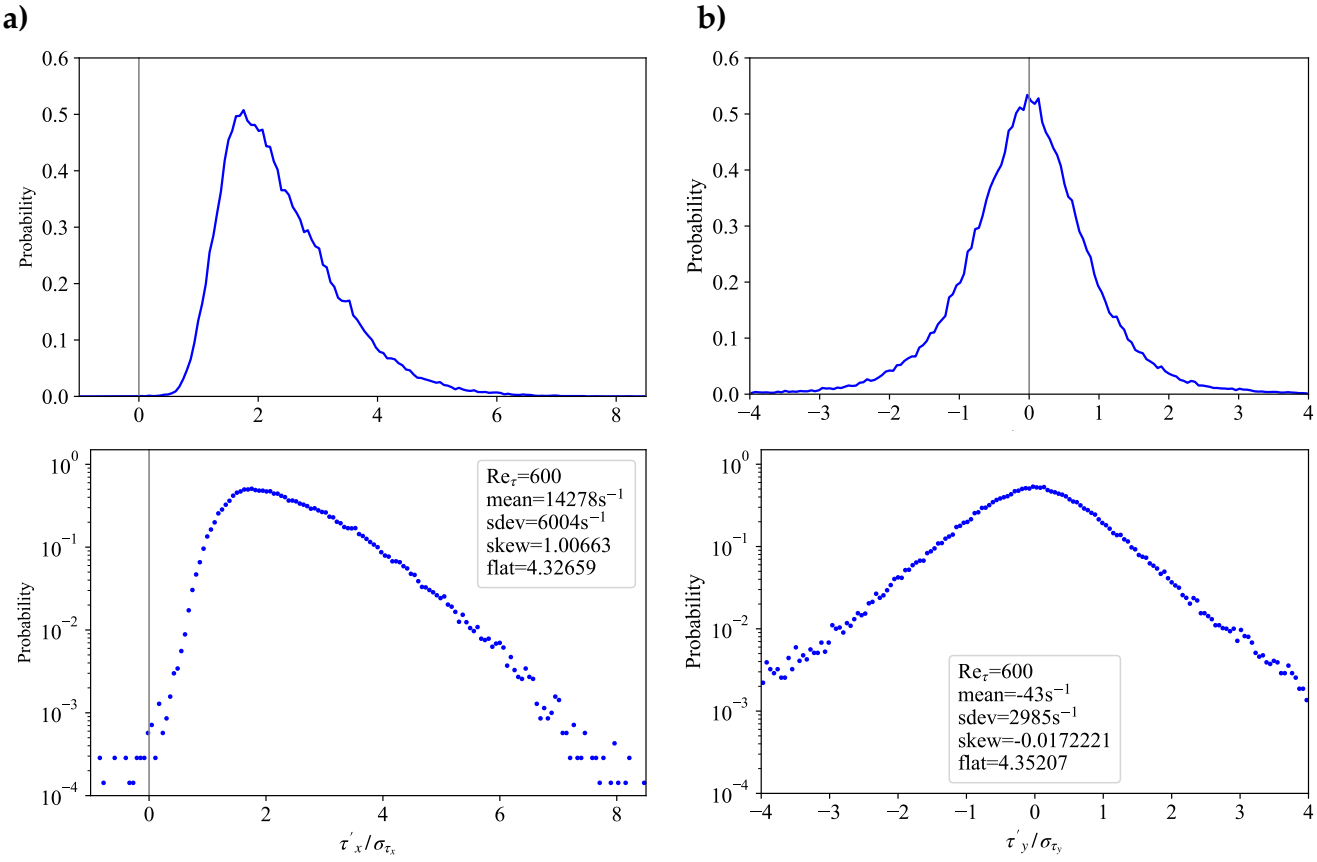

Figure 14. Streamwise (a) and spanwise (b) distributions of the wall shear rate at $\mathrm{Re}_0 = 48\,000$, $x = 14h$ as determined with MA-μPTV.

the same, so that neither the numerical effort for a geometrically constrained triplet fitting nor for a Voigt fitting seems to be needed. Despite significant deviations from the DNS in $\langle w'w' \rangle$ from $z^+ > 10$ (lines in faded colors), the data reconstructed with the Voigt fit is somewhat closer to the DNS compared to the other two variants.

Fig. 16b) shows similar consistency between MA-μPTV and DNS of a channel flow up to $z^+ = 28$ for the variances $\langle u'u' \rangle$, $\langle v'v' \rangle$ and $\langle u'w' \rangle$. The $\langle w'w' \rangle$ profile is consistently slightly above the profile from DNS to $z^+ \approx 10$, from which the profile shows larger deviations due to uncertainties in the depth position.

In addition, in Fig. 16b) fluctuations from profile-PIV were added for various final interrogation window sizes of $18.4\,l^+ \times 3.1\,l^+$ (48×8 pixels), $12.3\,l^+ \times 3.1\,l^+$ (32×8 pixels) and finally of $6.1\,l^+ \times 2.3\,l^+$ (16×6 pixels) using multi-correlation of 5 successive frames. These profiles indicate a weak influence of the window size on the height of the "inner peak", thus demonstrating the weak damping of the inner peak due to the finite window size. For comparison, at the "inner peak", the Kolmogorov length scale is $\eta \approx 2.4l^+$ (cf. Marusic et al., 2010), thus indicating that η is slightly undersampled with profile-PIV.

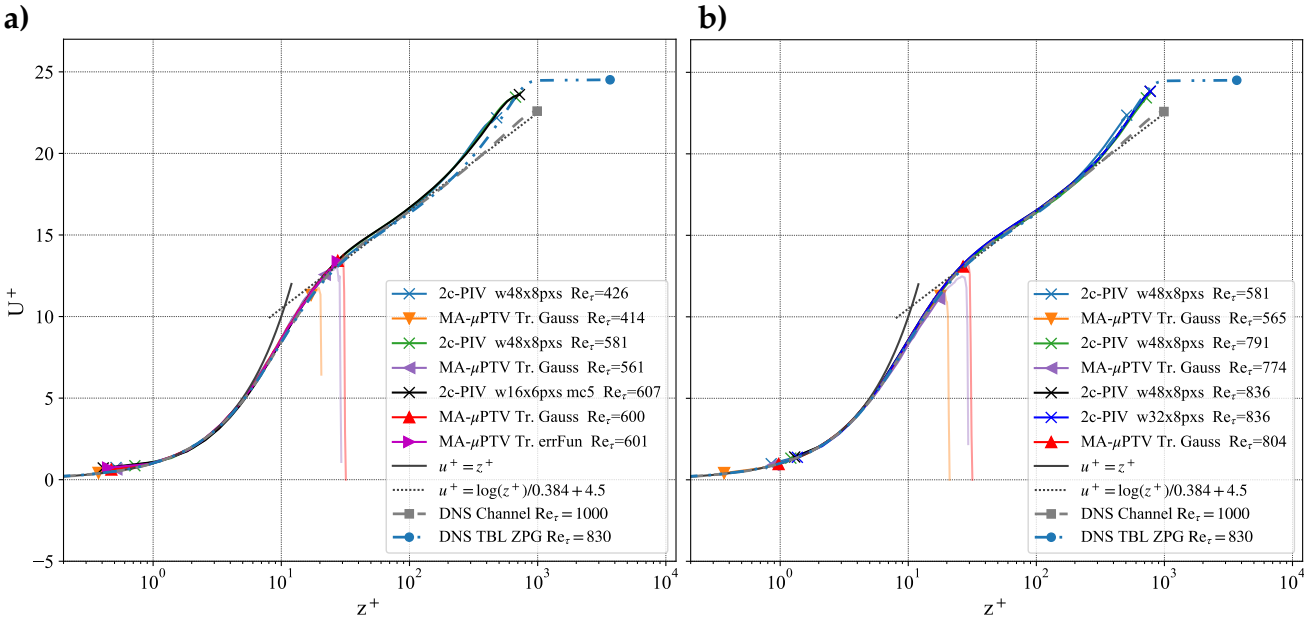

Figure 15. Mean streamwise velocity at $x = 14h$ (a) and at $x = 20h$ (b); Fading lines represent data were MA-μPTVfails in tracking velocities because particles are too far from focus.

10. Conclusions and outlook

The present results indicate that MA-μPTV is a viable non-contact technique for the measurement of the wall shear stress using a single access window accompanied by a relatively low instrumentation effort compared to multi-camera setups that require optical access from a multitude of directions. Using a 10W high-speed laser system and the present optical configuration allowed the capture of Lagrangian particle tracks in air in a ZPG-TBL up to a wall distance of 1 mm corresponding to 30 viscous units at the highest Reynolds number. The mean wall shear stress could be determined through a linear fit of the velocity gradient within the viscous sublayer ($z^+ < 4$) with an uncertainty of $\leq 1\%$ for all measured free stream conditions. Within the uncertainty of the flow parameters, the data is in good agreement with wall shear stress estimates obtained with single-row cross-correlation of the profile-PIV image data. The streamwise probability density distribution of the wall shear rate is inline with earlier experimental results and its standard deviation agrees well to correlations from literature. It is assumed that the reduced spanwise variations of the wall shear rate is related to the spanwise damping caused by the square cross-section of the wind tunnel. For the highest bulk Reynolds number, second order statistics from bin averaged velocities of all tracked particles indicate consistency with profile-PIV and agree well with DNS data up to wall distances of 28 viscous units ($0.88 - 0.92$ mm) for $\langle u'u' \rangle$, $\langle v'v' \rangle$ and $\langle u'w' \rangle$. The variance of the wall-normal component agrees well with both profile-PIV and DNS data up to a wall distance of 12 viscous units ($0.38 - 0.39$ mm). Measurements beyond this wall distance could potentially be achieved by a modified optical arrangement and increased laser power. Although it could be shown that the Voigt profile is better suited to reproduce the image intensities of the defocused particles from a wall distance of about 500 μm, this had little beneficial impact on the variance of

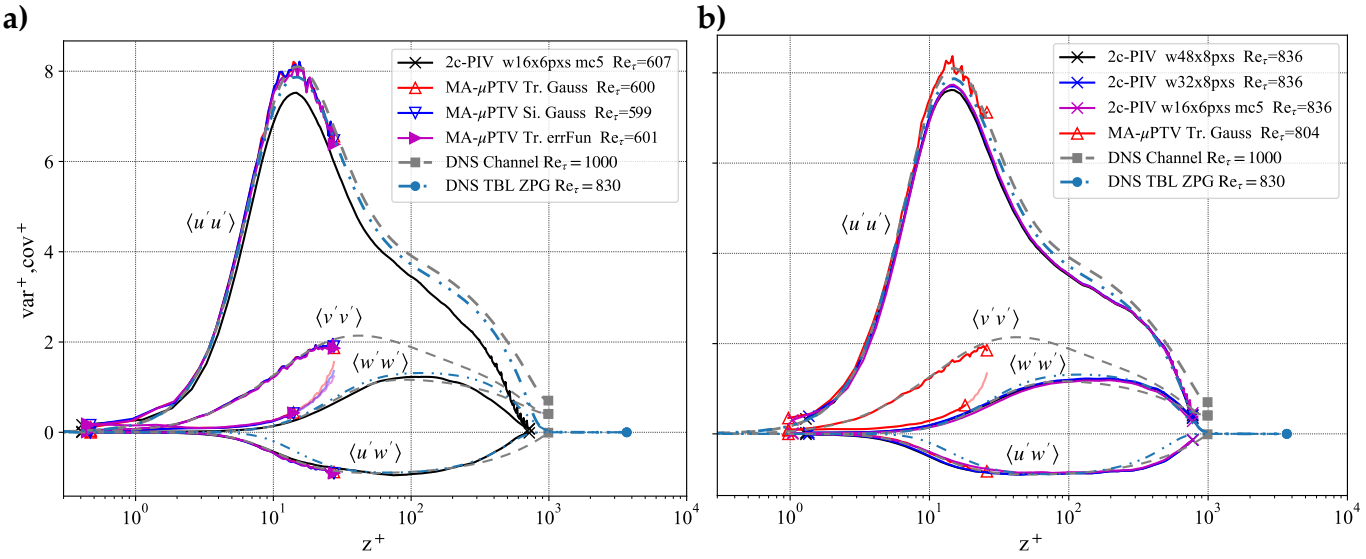

Figure 16. Variances and covariances of velocity at $\mathrm{Re}_0 = 48,000$, $x = 14h$ (left) and at $x = 20h$ (right); Fading lines represent the cut-off were $\langle w'w' \rangle$ raises strongly due to inaccuracies of the z position caused by too large a distance from focus.

the wall-normal velocity and other quantities. Overall, the results obtained with MA-µPTV are promising for potential applications requiring the measurement of near-wall flow properties with a low instrumental complexity or if only a single optical access is available.

Nomenclature

A, B, C	indices representing the center positions of each triplet image
b	displacement between triplet image centers
corrR-PIV	near-wall PIV evaluation based on cross-correlation of wall-parallel pixel rows
d, D	aperture diameter and spacing of triplet apertures
f	focal length
G	Gaussian profile
h	channel height / hydraulic diameter
l^+	viscous unit ν/u_τ
l^+_{min}	smallest expected viscous unit
L	Lorentzian profile
m	magnification
MA-µPTV	multi-aperture micro particle tracking velocimetry
PSF	point spread function
r	radius
s	search direction for adjacent corners of a triplet
t	time
u, v, w	velocity components in x, y, z
u^+, v^+, w^+	dimensionless velocities normalized with u_τ

V	Voigt profile
x, y, z	spatial coordinates
x^+, y^+, z^+	dimensionless spatial coordinates normalized with u_τ/ν
γ	half-width at full maximum of the Lorentzian
σ	width of a Gaussian/ standard deviation
η	Kolmogorov length scale
τ	wall shear stress
ν	kinematic viscosity
Re_0	Reynolds number based on bulk velocity and h
Re_τ	Reynolds number based on friction velocity and $h/2$
u_τ	friction velocity

References

Chen, S., Angarita-Jaimes, N., Angarita-Jaimes, D., Pelc, B., Greenaway, A. H., Towers, C. E., ... Towers, D. P. (2009). Wavefront sensing for three-component three-dimensional flow velocimetry in microfluidics. *Experiments in Fluids*, *47*, 849. Retrieved from https://doi.org/10.1007/s00348-009-0737-z doi: 10.1007/s00348-009-0737-z

Cierpka, C., Scharnowski, S., & Kähler, C. J. (2013). Parallax correction for precise near-wall flow investigations using particle imaging. *Applied Optics*, *52*(12), 2923–2931. Retrieved from https://opg.optica.org/ao/abstract.cfm?uri=ao-52-12-2923 (Publisher: Optica Publishing Group) doi: 10.1364/AO.52.002923

Cierpka, C., Segura, R., Hain, R., & Kähler, C. J. (2010). A simple single camera 3c3d velocity measurement technique without errors due to depth of correlation and spatial averaging for microfluidics. *Measurement Science and Technology*, *21*(4), 045401. Retrieved from https://doi.org/10.1088/0957-0233/21/4/045401 doi: 10.1088/0957-0233/21/4/045401

Diaz-Daniel, C., Laizet, S., & Vassilicos, J. C. (2017). Wall shear stress fluctuations: Mixed scaling and their effects on velocity fluctuations in a turbulent boundary layer. *Physics of Fluids*, *29*(5), 055102. Retrieved from https://aip.scitation.org/doi/10.1063/1.4984002 doi: 10.1063/1.4984002

Fuchs, C. J., Thomas; Kähler. (2019). Single axis volumetric μPTV for wall shear stress estimation. In *Proceedings of the 13th International Symposium on Particle Image Velocimetry.* Retrieved from https://athene-forschung.unibw.de/129386

Hutchins, N., & Choi, K.-S. (2002). Accurate measurements of local skin friction coefficient using hot-wire anemometry. *Progress in Aerospace Sciences*, *38*(4), 421–446. Retrieved from 10.1016/S0376-0421(02)00027-1 doi: 10.1016/S0376-0421(02)00027-1

Jones, O. C., Jr. (1976). An Improvement in the Calculation of Turbulent Friction in Rectangular Ducts. *Journal of Fluids Engineering*, *98*(2), 173–180. Retrieved from 10.1115/1.3448250 doi: 10.1115/1.3448250

Kumar, S. S., & Hong, J. (2018). Digital fresnel reflection holography for high-resolution 3d near-wall flow measurement. *Opt. Express*, *26*(10), 12779–12789. Retrieved from http://opg.optica.org/oe/abstract.cfm?URI=oe-26-10-12779 doi: 10.1364/OE.26.012779

Kumar, S. S., Huang, X., Yang, X., & Hong, J. (2021). Three dimensional flow motions in the viscous sublayer. *Theoretical and Applied Mechanics Letters*, *11*(2), 100239. Retrieved from https://www.sciencedirect.com/science/article/pii/S2095034921000465 doi: https://doi.org/10.1016/j.taml.2021.100239

Lee, M., & Moser, R. D. (2015). Direct numerical simulation of turbulent channel flow up to. *Journal of Fluid Mechanics*, *774*, 395–415. Retrieved from https://arxiv.org/abs/1410.7809 doi: 10.1017/jfm.2015.268

Malik, N. A., Dracos, T., & Papantoniou, D. A. (1993). Particle tracking velocimetry in three-dimensional flows. *Experiments in Fluids*, *15*(4), 279–294. Retrieved from https://doi.org/10.1007/BF00223406 doi: 10.1007/BF00223406

Marusic, I., Monty, J. P., Hutchins, N., & Smits, A. J. (2010). Spatial resolution and Reynolds number effects in wall-bounded turbulence. In *Proceedings of 8th international ERCOFTAC symposium on engineering turbulence modelling and measurements* (p. 10). Marseille, France. Retrieved from https://people.eng.unimelb.edu.au/imarusic/publications/Conferences/Marusic_ERCOFTAC_2010.pdf

Newville, M., Stensitzki, T., Allen, D. B., & Ingargiola, A. (2014). *LMFIT: Non-Linear Least-Square Minimization and Curve-Fitting for Python.* Zenodo. Retrieved from https://doi.org/10.5281/zenodo.11813 doi: 10.5281/zenodo.11813

Ouellette, N. T., Xu, H., & Bodenschatz, E. (2006). A quantitative study of three-dimensional Lagrangian particle tracking algorithms. *Experiments in Fluids*, *40*(2), 301–313. Retrieved from https://doi.org/10.1007/s00348-005-0068-7 doi: 10.1007/s00348-005-0068-7

Pereira, F., & Gharib, M. (2002). Defocusing digital particle image velocimetry and the three-dimensional characterization of two-phase flows. *Measurement Science and Technology*, *13*(5), 683. Retrieved from http://stacks.iop.org/0957-0233/13/i=5/a=305 doi: 10.1088/0957-0233/13/5/305

Rossi, M. (2020). Synthetic image generator for defocusing and astigmatic PIV/PTV. *Measurement Science and Technology*, *31*(1), 017003. Retrieved from 10.1088/1361-6501/ab42bb doi: 10.1088/1361-6501/ab42bb

Schanz, D., Gesemann, S., Schröder, A., Wieneke, B., & Novara, M. (2013). Non-uniform optical transfer functions in particle imaging: calibration and application to tomographic reconstruction. *Measurement Science and Technology*, *24*(2), 024009. Retrieved from http://stacks.iop.org/0957-0233/24/i=2/a=024009 doi: 10.1088/0957-0233/24/2/024009

Schlatter, P., & Örlü, R. (2010). Assessment of direct numerical simulation data of turbulent boundary layers. *Journal of Fluid Mechanics*, *659*, 116–126. Retrieved from https://www.cambridge.org/core/journals/journal-of-fluid-mechanics/article/assessment-of-direct-numerical-simulation-data-of-turbulent-boundary-layers/A3F3653249AEAC86A13E7E37B6FDABCD (Publisher: Cambridge University Press) doi: 10.1017/S0022112010003113

Schreier, F. (2019). Notes: An assessment of some closed-form expressions for the Voigt function III: Combinations of the Lorentz and Gauss functions. *Journal of Quantitative Spectroscopy and Radiative Transfer*, *226*, 87–91. Retrieved from https://www.sciencedirect.com/science/article/pii/S0022407318309452 doi: 10.1016/j.jqsrt.2019.01.017

Sheng, J., Malkiel, E., & Katz, J. (2008). Using digital holographic microscopy for simultaneous measurements of 3D near wall velocity and wall shear stress in a turbulent boundary layer. *Experiments in Fluids*, *45*(6), 1023–1035. Retrieved from 10.1007/s00348-008-0524-2 doi: 10.1007/s00348-008-0524-2

Weideman, J. a. C. (1994). Computation of the Complex Error Function. *SIAM Journal on Numerical Analysis*, *31*(5), 1497–1518. Retrieved from https://epubs.siam.org/doi/10.1137/0731077 doi: 10.1137/0731077

Willert, C. (2015). High-speed particle image velocimetry for the efficient measurement of turbulence statistics. *Experiments in Fluids*, *56*(1), 17. Retrieved from http://link.springer.com/10.1007/s00348-014-1892-4 doi: 10.1007/s00348-014-1892-4

Willert, C., & Gharib, M. (1992). Three-dimensional particle imaging with a single camera. *Experiments in Fluids*, *12*(6), 353–358. Retrieved from https://link.springer.com/article/10.1007/BF00193880 doi: 10.1007/BF00193880

Willert, C., Novara, M., Schanz, D., Geisler, R., Schroll, M., Ribergard, S., & Schröder, A. (2021). Multi-resolution, time-resolved PIV measurements of a Decelerating Turbulent Boundary Layer near Separation. *14th International Symposium on Particle Image Velocimetry*, *1*(1). Retrieved from https://ispiv21.library.iit.edu/index.php/ISPIV/article/view/77 doi: 10.18409/ispiv.v1i1.77

Willert, C., Soria, J., Cuvier, C., Foucaut, J. M., & Laval, J. P. (2018). Flow reversal in turbulent boundary layers with varying pressure gradients. Lisbon, Portugal. Retrieved from http://www.lisbon-lasersymposium.org/lxlaser2018

Örlü, R., & Schlatter, P. (2011). On the fluctuating wall-shear stress in zero pressure-gradient turbulent boundary layer flows. *Physics of Fluids*, *23*(2), 021704. Retrieved from 10.1063/1.3555191 doi: 10.1063/1.3555191